Nickel- and Ruthenium-Doped Lanthanum Chromite Anodes: Effects of Nanoscale Metal Precipitation on Solid Oxide Fuel Cell Performance

W. Kobsiriphat,* B. D. Madsen, Y. Wang, M. Shah, L. D. Marks, and S. A. Barnett*,z

Department of Materials Science, Northwestern University, Evanston, Illinois 60208, USA

This paper compares the effects of Ni and Ru dopants in lanthanum chromite anodes by correlating structural characterization and electrochemical measurements in solid oxide fuel cells (SOFCs). Transmission electron microscope observations showed that nanoclusters of Ni or Ru metal precipitated onto lanthanum chromite ($La_{0.8}Sr_{0.2}Cr_{1-y}X_yO_{3-\delta}$, X = Ni,Ru) surfaces, respectively, after exposure to hydrogen at 750–800°C. Ni nanoclusters were typically $\sim$10 nm in diameter immediately after reduction and coarsened to $\sim$50 nm over $\sim$300 h at 800°C. In contrast, Ru cluster size was stable at $\leq$5 nm, and the cluster density was >10 times larger. SOFC tests were done with the doped lanthanum chromite anodes on $La_{0.9}Sr_{0.1}Ga_{0.8}Mg_{0.2}O_{3-\delta}$ electrolyte-supported cells. Ni nanocluster nucleation improved cell performance and reduced anode polarization resistance compared to cells with undoped ($La_{0.8}Sr_{0.2}CrO_{3-\delta}$) anodes, but the improvement was much less than that for Ru. This comparison suggests that the smaller size of the Ru nanoclusters played an important role in enhancing anode electrochemical kinetics.
© 2009 The Electrochemical Society.   [DOI: 10.1149/1.3269993] All rights reserved.

Nanometer-scale electrode structures in solid oxide fuel cells (SOFCs) have the potential to yield improved performance due to increased surface areas[1] and triple-phase boundary lengths.[2] However, there are still questions as to the long-term stability of nanoscale materials at SOFC operating temperatures that can range from 500 to 1000°C.[3,4] Clearly, nanoparticles may coarsen at the relatively high firing temperatures ($\sim$1400°C) used to process SOFCs. Thus, nanoparticles must be introduced after high temperature firing steps.

A new method for introducing nanoscale metal particles into oxide anodes was recently reported. The oxide material, $La_{0.8}Sr_{0.2}Cr_{1-y}Ru_yO_{3-\delta}$ (LSCrRu), was fired in air at elevated temperature, but when the anode was reduced during the initial SOFC operation, Ru nanoparticles <5 nm in diameter formed on the oxide surface.[5,6] The anode polarization resistance decreased substantially as the nanoparticles formed, but then remained relatively constant. A similar effect was reported for anodes containing $La_{0.8}Sr_{0.2}Cr_{1-y}Ni_yO_{3-\delta}$ (LSCrNi), although the Ni nanoparticles were larger (>10 nm) than the Ru particles, and the decrease in polarization resistance was relatively small.[7]

Here we present a detailed study of the LSCrNi anode structure and electrochemical performance, and contrast the results with those for LSCrRu. The aim was to better understand the role that metal nanocluster composition and size plays in electrode polarization, and also to explore the stability of metal nanoclusters under SOFC operating conditions. Ni is a lower cost alternative to Ru in these anodes, although it is more susceptible to sintering and coking.[8]

Experimental Procedures

Powders of LSCrRu and LSCrNi were synthesized by solid-state reaction at 1200°C for 3 h, yielding particle sizes of $\sim$1 to 2 μm. In the discussion below, the different Ni or Ru contents are given, for example, as LSCrNi31 ($La_{0.8}Sr_{0.2}Cr_{0.69}Ni_{0.31}O_{3-\delta}$). The SOFC anodes consisted of 50 wt % of one of the above chromite powders mixed with 50 wt % Gd-doped ceria (GDC).

All SOFCs utilized $La_{0.9}Sr_{0.1}Ga_{0.8}Mg_{0.2}O_{3-\delta}$ (LSGM) electrolytes, $\sim$400 μm thick. The LSGM powders were fabricated via solid-state reaction at 1250°C, followed by uniaxial pressing and sintering for 6 h at 1450°C to form the electrolyte pellets. The cathodes were $La_{0.6}Sr_{0.4}Co_{0.2}Fe_{0.8}O_{3-\delta}$ (LSCF) mixed with 50 wt % GDC. The anodes and cathodes (0.5 cm^2 active area, $\sim$25 μm

thick) were screen printed on the LSGM electrolytes and fired for 3 h at 1200 and 1000°C, respectively. Au current collector grids were screen printed over the electrodes and contacted using Ag wires.

Single cell tests were performed as described previously[9] using a four-wire setup for current–voltage (*I-V*) and electrochemical impedance spectroscopy (EIS) measurements (BAS-Zahner IM-6). In life tests, the cells were first stabilized at temperature with Ar at the anode before starting H$_2$ flow. The H$_2$ flow to the cells was first humidified by bubbling the gas through H$_2$O at room temperature, resulting in $\approx$3% H$_2$O in H$_2$. Times given in life test results are after the start of humidified H$_2$ flow. Measurements on various other SOFCs indicated that Ar was almost entirely purged from the anode compartment before the first electrical measurements (15 min).

X-ray diffraction measurements of anode powders were done with a standard diffractometer (Rigaku 0.8 kW Dmax). Scanning electron microscopy (SEM) measurements were done along with energy-dispersive spectroscopy (EDS) (Hitachi S3400N-II, S3500, S3800, and S4800-II cFEG). High resolution electron microscopy (HREM) studies were carried out on the powder samples using a JEOL JEM-2100F electron microscope operated at 200 kV. The powders were annealed in either dry H$_2$ or 3% H$_2$O/H$_2$. Micrographs were digitally acquired on a 2 × 2 k charge-coupled device camera using a Gatan Imaging Filter system. A small amount of powder was added to acetone, followed by ultrasonic mixing to achieve a particle dispersion. A drop of the resulting suspension was deposited on carbon-coated transmission electron microscope (TEM) grids (Ted Pella). Samples were stored in a desiccator overnight before HREM examination.

Experimental Results

The following sections describe first the structural observations of LSCrNi, with results for LSCrRu included for comparison. In the second section, electrochemical test results for SOFCs with these anodes are discussed.

Structural characterization.— Ni-doped anodes.— Figure 1 shows typical X-ray diffraction patterns from as-prepared LSCrNi31 powder and after annealing in H$_2$ at 800°C for 3, 45, and 312 h. The main peaks all matched well with those expected for $La_{0.8}Sr_{0.2}CrO_3$ (JCPDS no. 74-1980); this is not surprising because the addition of Ni gives a relatively small shift in lattice parameter that was not resolvable in these X-ray measurements. However, a peak likely corresponding to NiO was present in the as-prepared powder. This indicates that the 31 mol % Ni was in excess of the solubility limit. The NiO peak was replaced by a Ni peak after reduction. X-ray data

* Electrochemical Society Active Member.
z E-mail: s-barnett@northwestern.edu
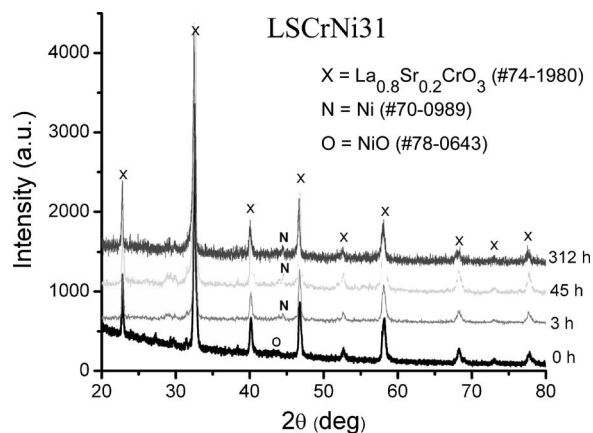
Figure 1. X-ray diffraction pattern of LSCrNi31 powders as-prepared and reduced for 3, 45, and 312 h at 800°C.

for a powder with lower Ni content, LSCrNi13, were similar to that in Fig. 1, but Ni and NiO peaks were not observed. This suggests that the 13% Ni was below the solubility limit in the chromite phase within the sensitivity of the X-ray measurement of ≈ 3 mol %.

A shoulder or small peak was observed at the low angle side of some of the lanthanum chromite peaks. This is most easily seen for the strongest peak at $\sim 32.6°$. This may be due to a partial shift from a cubic lattice to one with lower symmetry, such as an orthorhombic lattice. For example, the orthorhombic $LaCrO_3$ structure (JCPDS no. 83-1327) has strong peaks at $32.61°$ (121) and $32.68°$ (200). Note also that small peaks were observed between $2\theta = 25$ and $30°$, suggesting the minor presence of secondary phases, of which the identities were not determined.

Figure 2 shows an LSCrNi18–GDC anode before the SOFC testing observed by SEM and EDS mapping of La, Ce, and Ni. LSCrNi and GDC particles are readily resolved in the EDS maps as indicated by the spatial modulations of the La and Ce peak intensities. Although the Ni peak intensity mostly tracked that of La, as ex-
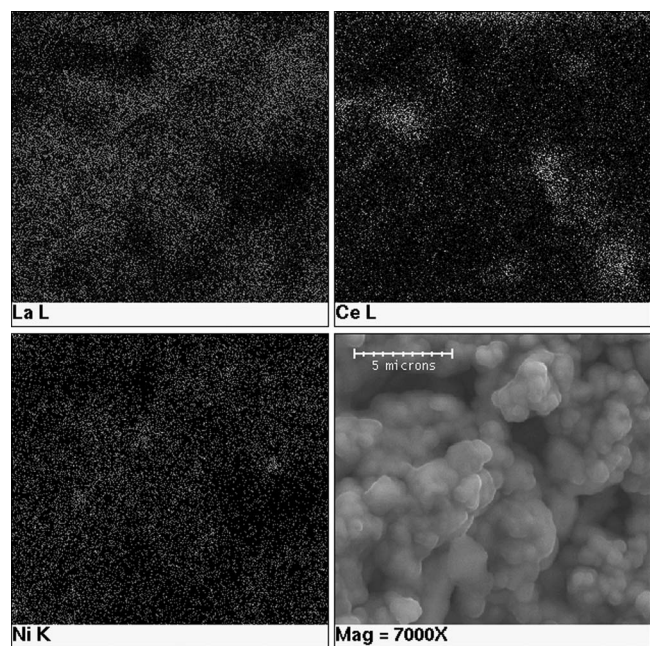

Figure 2. SEM image (bottom right) and EDS maps obtained from the La Lα_1, Ce Lα_1, and Ni Kα_1 peaks of an LSCrNi18 anode before the SOFC operation.
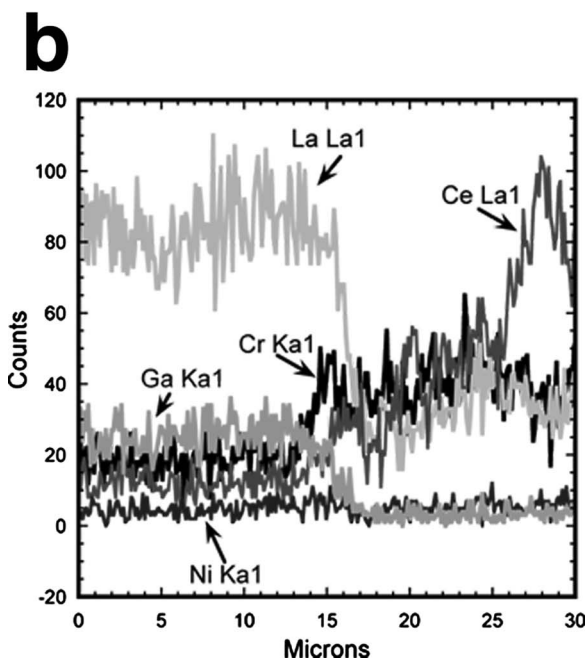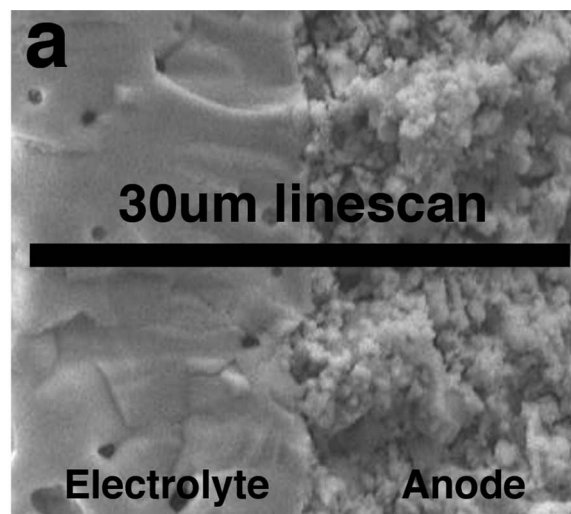
Figure 3. Cross-sectional SEM image at the LSGM electrolyte/LSCrNi18 anode interface (a) showing the position of the intensity line scan from La, Ce, Cr, Ga, and Ni signals shown in (b).

pected for Ni distributed uniformly within the lanthanum chromite lattice, there were a few areas where the Ni signal was relatively high. This shows that a fraction of the Ni was present as a separate phase, presumably NiO. This suggests that the solubility limit of Ni in $La_{0.8}Sr_{0.2}CrO_{3-\delta}$ was < 18 mol % and, combined with the above X-ray diffraction data, suggests a solubility limit between 13 and 18 mol %.

Figure 3a shows a fracture cross-sectional SEM image from a typical LSCrNi18–GDC anode at the interface with the LSGM electrolyte. Figure 3b shows an intensity line scan taken while translating the beam across the electrolyte/anode interface. The SEM image shows the porous anode structure and a fairly dense electrolyte with good anode/electrolyte contact. The line scan indicated that the main anode and electrolyte components were retained in their respective layers, although there did appear to be some interdiffusion within ~ 1 µm of the interface. Furthermore, the Cr signal was most intense within the anode, but some intensity was seen in the LSGM electrolyte, suggesting that Cr diffusion may have been more extensive. The Ni intensity was too low to assess. Note that La-doped
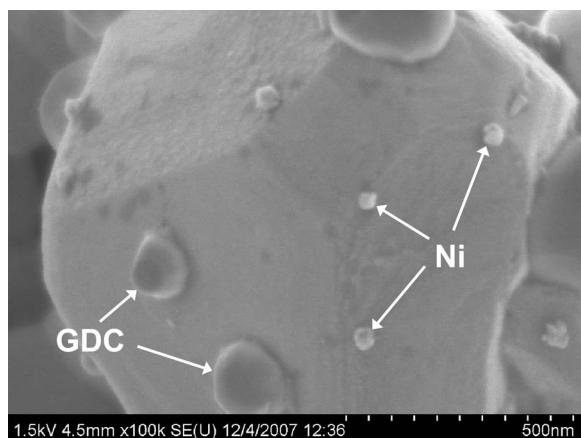
Figure 4. Higher resolution SEM image of an LSCrNi18 particle after a reduction at 800°C for 312 h in humidified hydrogen. The larger particles are GDC ($\approx$100 to 200 nm diameter), and the smaller particles are Ni (30–50 nm diameter).

ceria barrier layers are normally used between Ni–yttria-stabilized zirconia (YSZ) anodes and LSGM electrolytes to prevent Ni–LSGM reactions and possible La out-diffusion from the LSGM electrolyte.[10] Figure 3 suggests that this may also be a useful expedient for the present LSCrNi anodes.

Figure 4 shows a higher resolution SEM image of an individual LSCrNi particle in an LSCrNi18–GDC anode after the SOFC operation for 312 h at 800°C in humidified hydrogen fuel. The LSCrNi particle was faceted and decorated with what appears to be GDC particles (100–200 nm diameter) and smaller Ni particles ($\sim$50 nm diameter).

Figure 5 shows TEM images from LSCrNi31 powders both in the as-prepared state and after reduction for 3, 45, and 311 h at 800°C in dry hydrogen fuel. The as-prepared powder showed no nanoparticles on the lanthanum chromite surface (Fig. 5a). After 3 h of reduction, hemispherical Ni particles 10–15 nm in diameter were observed (Fig. 5b). The outer shell seen on the top Ni particle of Fig. 5b was determined by the lattice fringe spacing measurements to be NiO. The nanoparticles were presumably Ni metal during anode
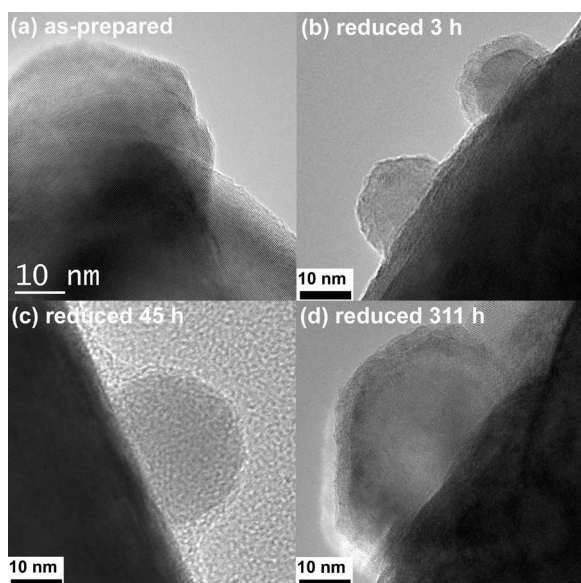
Figure 5. TEM images obtained from LSCrNi31 powder (a) as-prepared, (b) reduced at 800°C for 3, (c) 45, and (d) 311 h in dry hydrogen.
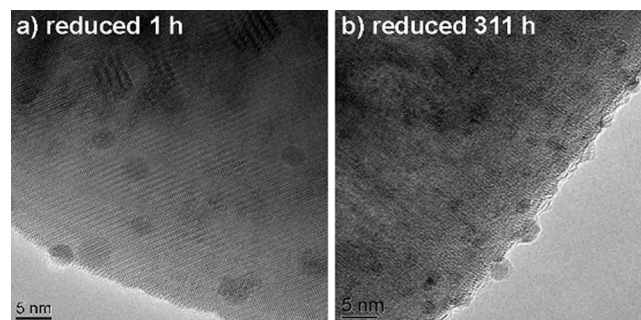

Figure 6. High resolution TEM images of LSCrRu18 particle surfaces after reduction at 800°C for (a) 1 h in humidified H_2 and (b) 311 h in dry H_2, showing nanoclusters on the surface.

operation in hydrogen fuel; the oxide shell was an artifact that formed after the anode was exposed to air. After 311 h of reduction (Fig. 5d), the Ni particles had grown significantly to an average hemisphere diameter of 50–60 nm. The size and density of the Ni particles in Fig. 5d were consistent with the SEM image (Fig. 4) from LSCrNi annealed under similar conditions.

Ru-doped anodes.— The SEM microstructure of the LSCrRu–GDC anodes was generally similar to that shown in Fig. 1-3 for LSCrNi–GDC.[6] Figure 6 shows images of LSCrRu18 examined by TEM after exposure to H_2 at 800°C for comparison with the LSCrNi31 in Fig. 5. The unreduced LSCrRu showed no evidence of any nanoparticles.[6] After 1 h reduction in humidified hydrogen, $\leq$5 nm diameter Ru nanoparticles were readily apparent on the LSCrRu surfaces (Fig. 6a). After 311 h (Fig. 6b) at 800°C in the dry hydrogen, the size and density of Ru nanoparticles had not changed significantly. The diameter of Ru particles did not exceed 10 nm even after 1000 h of reduction.[6]

SOFC test results.— *Ni-doped anodes.*— Figure 7 shows typical *I-V* curves, measured at various times at 750°C, from an SOFC with an LSCrNi18–GDC anode. The cell performance gradually improved during the first $\sim$50 h of cell operation, with the maximum power density increasing from 120 to 175 mW/cm². The power density then began to decrease very gradually. The maximum power density measured at 800°C was 364 mW/cm².

Figure 8 shows a set of EIS scans taken at various times during a life test at 750 and 800°C for a cell with an LSCrNi18–GDC anode. The high frequency intercepts were attributed to the ohmic resistance associated with the 0.4 mm thick LSGM electrolyte.[11] Separate symmetric-cell measurements of the LSCF–GDC cathodes yielded a relatively small polarization resistance of <0.1 Ω cm²[12]
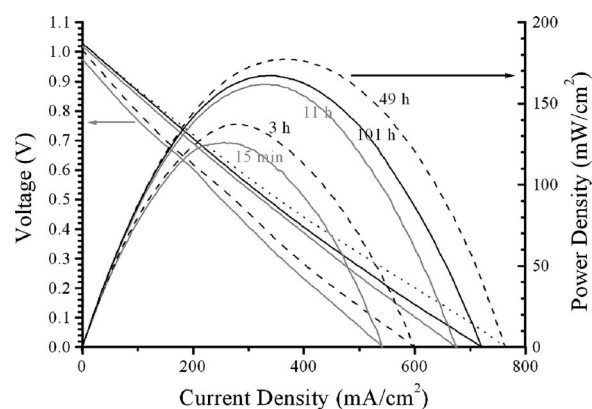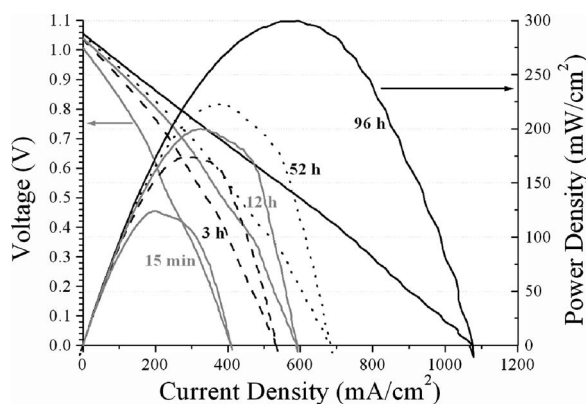

Figure 7. Voltage and power density vs current density at 750°C, measured at various times after the start of humidified H_2 flow for a typical cell with an LSCrNi18–GDC anode.
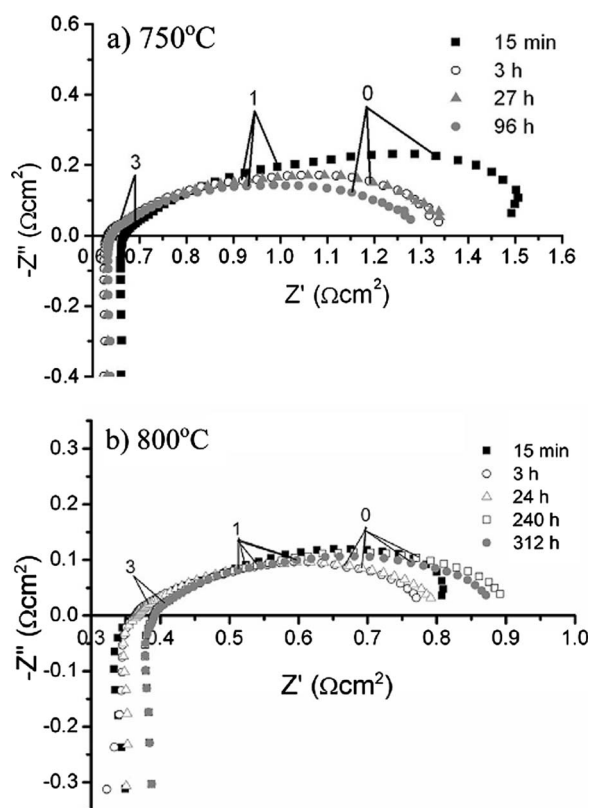
Figure 8. Impedance spectra measured from a cell with an LSCrNi18–GDC anode at OCV at different times at (a) 750 and (b) 800°C. Frequencies (10^x Hz) for the impedance data are denoted for several data points.

at these temperatures, indicating that the polarization arcs were primarily due to the anode. At 750°C, there was a substantial decrease in the polarization arc during the first 3 h, but little improvement over the next 100 h. At 800°C, there was a slight performance improvement during the first 3 h of testing, but then a gradual increase over longer times.

Ru-doped anodes.— Figure 9 shows the *I-V* curves for a typical SOFC with an LSCrRu–GDC anode at various times after the onset of testing in humidified H_2 at 750°C. The maximum power density within the first ≈ 15 min of testing was ≈ 125 mW/cm^2 and increased continuously with time, reaching 300 mW/cm^2 at 100 h. After this, the power density stabilized. Similar results were ob-

Figure 9. Voltage and power density vs current density at 750°C, measured at various times after the start of humidified H_2 flow, for a typical cell with an LSCrRu18–GDC anode.
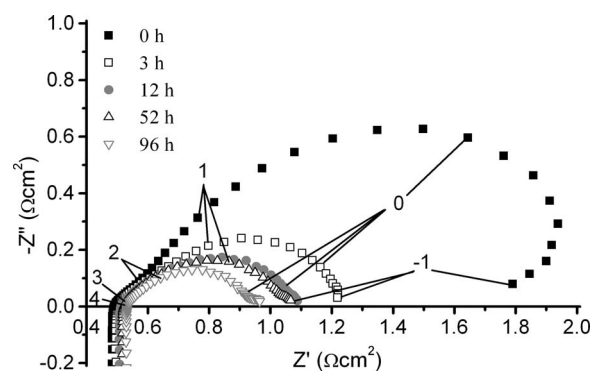
Figure 10. Electrochemical impedance spectra for a cell with an LSCrRu18–GDC anode at 750°C and OCV after exposure to the humidified hydrogen for increasing time. Frequencies (10^x Hz) for the impedance data are denoted for several data points.

served at other test temperatures, e.g., at 800°C, the power increased from 250 mW/cm^2 (15 min) to $\sim$400 mW/cm^2 (3 h).[7] Figure 10 shows electrochemical impedance spectra taken at 750°C and open-circuit voltage (OCV) at various times after hydrogen exposure. High frequency intercepts were again at ≈ 0.5 Ω cm^2 and attributed to the ohmic resistance associated with the thick LSGM electrolyte. The low frequency arc, initially ≈ 1.5 Ω cm^2, decreased rapidly before stabilizing at ≈ 0.4 Ω cm^2, indicating that the power density increase with time was an electrode effect. Although the initial power density and impedance values were approximately the same as those shown in Fig. 7 and 8a for the SOFC with LSCrNi anode, the improvement was much greater for LSCrRu.

Discussion

Dynamics of metal nanoparticle nucleation.— Prior reports on the possibility of Ni nanoparticle nucleation on Ni-containing oxides have shown mixed results. Ni nanoparticles were observed on YSZ surfaces in Ni–YSZ anodes after exposure of the anodes to hydrogen at elevated temperature.[13-15] It was suggested that a small amount of Ni solubilized in the YSZ phase during firing of the Ni–YSZ in air and that this Ni subsequently segregated out of the Ni upon reduction. The reported Ni nanocluster sizes and densities were similar to those shown in Fig. 4. Similarly, Sfeir et al.[16] observed Ni islets (20–50 nm particle size) by TEM after performing catalytic tests on $La_{0.85}Ca_{0.15}Cr_{0.9}Ni_{0.1}O_3$ powders in CH_4:Ar:H_2O gas mixtures. However, Ni particles were not observed by TEM in $LaCr_{0.9}Ni_{0.1}O_3$ powders after a catalytic testing. It is possible that the solubility limit of Ni in the chromite lattice was different in the cases of A-site doped chromites. Sauvet and Irvine[17] observed the agglomeration of Ni in SEM–EDS maps after methane reforming measurements on $La_{0.70}Sr_{0.30}Cr_{0.95}Ni_{0.05}O_3$ at 750–850°C, suggesting the nucleation of metallic Ni particles.

In the following, we attempt to explain the nanoparticle nucleation and growth based on a simple model[5,7] that is in accord with prior studies of metal precipitation from oxides.[18-20] Briefly, a metal bulk diffusion from within the chromite particles to the surface is driven by the free-energy decrease associated with the reduction in oxidized Ni (in LSCrNi) to Ni metal. Prior thermodynamic calculations[21] showed that Ni is unstable in the $LaCrO_3$ lattice at 800°C and $pO_2 < \sim 10^{-14}$ atm; pO_2 in the present experiments was $\sim 10^{-20}$ atm. Surface metal atoms arriving at the chromite free surface nucleate clusters because of poor wetting. Note that internal metal precipitation[18,20] was not observed in any of the TEM observations.

Observations of the amount of metal accumulated on the chromite surface allow an estimation of the bulk diffusion coefficient.[5] Based on the TEM images after 45 h of reduction at 800°C (Fig. 5), the density of Ni nanoparticles was $\sim$5

$\times 10^{13}$ m^{-2}; this was $\sim$1000 times smaller than the Ru particle density in LSCrRu under the same conditions ($\sim 4 \times 10^{16}$ m^{-2}).[5] The diameter of the Ni particles was $\sim$25 nm compared to $\sim$3 nm for Ru particles, a factor of $\sim$10 times higher, such that the Ni volume per particle was $\sim$1000 times higher. That is, the net amounts of surface Ni and Ru, per unit area of chromite particle surface, were similar, $\sim$20 atoms/nm^2. Assuming that the amount of metal accumulated on the oxide surface was limited primarily by bulk diffusion,[22] this indicates that the Ni and Ru diffusion coefficients in the chromite were similar. Given that the Ni or Ru atomic densities in the LSCrNi18 and LSCrRu18 were $\sim$1 atom/nm^3, obtaining the measured metal surface concentrations required diffusion from a depth L of $\sim$20 nm below the chromite surface. Using this approximate diffusion length and a diffusion time $t = 45$ h, a diffusion coefficient $D \sim L^2/t \sim 10^{-21}$ m^2 s^{-1} was obtained. This value is consistent with the reported cation bulk diffusion coefficients in lanthanum chromite extrapolated to 800°C.[23] As discussed elsewhere,[6] continuing Ni/Ru out-diffusion yields an increasingly nonstoichiometric (La- and Sr-rich) chromite; there may be a limit on the fraction of Ni or Ru that can be removed, such that cations must diffuse from deeper within the chromite particle. That is, the above diffusion coefficient is a lower limit.

Although the rate of Ni segregation to the surface was similar to that observed for Ru, the Ni nanoparticle size was larger and the density smaller. This difference is presumably explained by a combination of thermodynamic and kinetic factors that affect nucleation. Although the thermodynamic factors are difficult to assess because of the lack of data for these doped chromites, the kinetics can be discussed qualitatively. That is, the lower Ni nucleus density may be due, at least in part, to faster surface diffusion of Ni than Ru. Faster Ni diffusion on the chromite surface would allow nuclei to be fed by adatoms from larger areas, yielding larger and more widely spaced nuclei, analogous to thin-film nucleation.[24] The more rapid coarsening of Ni particles, compared to Ru particles, may also indicate larger Ni diffusivities. Although data on the diffusivities of Ni and Ru on chromite surfaces are not available, Ni has a lower melting point (1455°C) than Ru (2334°C), which may suggest a higher surface diffusivity.

Anode electrochemical performance.— The time frame over which the power density increased was similar for cells with LSCrNi18 and LSCrRu18. At 750°C, the cell performance reached a maximum at $\sim$50 h for Ni and $\sim$100 h for Ru. At 800°C, the performance reached a maximum within the first few hours of operation in both cases. This is consistent with the idea that Ni and Ru out-diffusion rates were similar, leading to peak nanoparticle densities at similar times. For Ni, the anode performance at 800°C decreased noticeably after the peak, presumably due to the substantial coarsening of the Ni particles. This is in contrast to the results for Ru, where the nanoparticle size and density remained more stable resulting in a fairly stable polarization resistance. For LSCrNi31 anodes, no initial increase in performance was observed (the initial performance was similar). This was probably due to the presence of a NiO phase before the reduction (see the Experimental Results section), which should reduce very rapidly to Ni upon exposure to H$_2$.

The electrochemical performance improvement due to Ni was less than for Ru. The smallest polarization resistance R_p measured for LSCrNi18–GDC was 0.38 Ω cm^2, approximately twice the minimum R_p achieved from a cell with LSCrRu18–GDC anode. Given that both metals have been shown to be very effective SOFC anode electrocatalysts,[25] the difference is presumably attributable to their different morphologies. As noted in the beginning of the Discussion section, the Ni particles were typically $\sim$10 times the diameter of Ru clusters under comparable conditions, but the particle density was $\sim$1000 times less. The higher R_p of the LSCrNi-based anodes can be explained by postulating that the resistance was inversely proportional to the total metal surface area, which was $\sim$10 times lower for Ni compared to Ru (0.02 nm^2 Ni per nm^2 of

LSCrNi compared to 0.28 nm^2 Ru per nm^2 of LSCrRu). Physically, this would be expected in a case where the metal surface provides sites for H$_2$ dissociation followed by a spillover onto the oxide surface. Note that R_p was previously shown to correlate inversely with the total Ru nanoparticle surface area on LSCrRu anodes.[6] An alternative assumption that the polarization resistance depends inversely on the total perimeter length of the particle-oxide contacts, i.e., the three-phase boundary (TPB) length, is also possible. This also predicts a higher R_p for the Ni case, with a TPB length of 0.0035 nm/nm^2 in the LSCrNi case compared to 0.38 nm/nm^2 of LSCrRu.

The present results can be compared with prior results on similar anodes. First, SOFCs identical to the above but with LSCr–GDC anodes were previously tested,[6] primarily at 800°C. The form of the *I-V* curves and the EIS spectra was similar to those shown above for LSCrNi and LSCrRu anode cells. Although the power density increased over time before stabilizing, maximum power densities were lower (170–240 mW/cm^2 at 800°C) than for cells with LSCrRu and LSCrNi anodes. The minimum polarization resistance (at 800°C, OCV), 0.5–0.75 Ω cm^2, was higher than that for the LSCrRu–GDC (0.13 Ω cm^2) and LSCrNi–GDC (0.4 Ω cm^2) anodes. Second, cells with (La,Sr)(Cr,V)O$_3$–GDC–Ni (LSCrV–GDC–Ni) anodes, in which Ni was incorporated as a separate micrometer-scale NiO powder rather than in LSCrNi, were previously reported.[12] Comparing the present LSCrNi18–GDC anode with the LSCrV–GDC–Ni anode with the same net Ni content, 3 wt %, the LSCrNi18–GDC anode had lower polarization resistance, $\approx$0.4 Ω cm^2, than LSCrV–GDC–Ni, $\approx$0.5 Ω cm^2. The lower resistance of the present anodes was presumably due to the larger surface area of the nanometer-scale Ni particles compared to the micrometer-scale Ni particles in the LSCrV–GDC–Ni anodes.

Conclusions

Based on the results from the microstructural and electrochemical characterization, the following conclusions were drawn regarding LSCrNi–GDC anodes.

1. The solubility limit of Ni in the chromite was $\sim$13 to 18 mol %; compositions with higher Ni content showed a separate NiO phase.

2. Ni nanoparticles were observed on LSCrNi surfaces upon reduction but were substantially larger with a lower density than Ru particles on LSCrRu. This observation was tentatively explained by a higher diffusivity of Ni adatoms on the chromite surface.

3. SOFCs with LSCrNi–GDC anodes showed an improved performance compared to LSCr–GDC anodes, indicating that Ni nanoclusters had an electrocatalytic effect.

4. The performance of SOFCs with LSCrNi–GDC anodes was significantly worse than those with LSCrRu–GDC anodes, a difference attributed to the larger size and lower density of the Ni particles.

5. SOFCs with LSCrNi–GDC anodes showed poor stability at 800°C over $\approx$300 h with a cell performance degrading gradually over time. TEM images revealed a probable reason for this effect, gradual coarsening of the Ni nanoparticles.

Acknowledgments

References

1. S. B. Adler, J. A. Lane, and B. C. H. Steele, *J. Electrochem. Soc.*, **143**, 3554 (1996).
2. J. R. Wilson, W. Kobsiriphat, R. Mendoza, H.-Y. Chen, J. M. Hiller, D. J. Miller,

K. Thornton, P. W. Voorhees, S. B. Adler, and S. A. Barnett, *Nature Mater.*, **5**, 541 (2006).
3. A. J. McEvoy, *Solid State Ionics*, **132**, 159 (2000).
4. Z. Zhan and S. A. Barnett, *Solid State Ionics*, **176**, 871 (2005).
5. B. D. Madsen, W. Kobsiriphat, Y. Wang, L. D. Marks, and S. A. Barnett, *J. Power Sources*, **166**, 64 (2007).
6. W. Kobsiriphat, B. D. Madsen, Y. Wang, L. D. Marks, and S. A. Barnett, *Solid State Ionics*, **180**, 257 (2009).
7. B. D. Madsen, W. Kobsiriphat, L. D. Marks, Y. Wang, and S. A. Barnett, in *Tenth International Symposium on Solid Oxide Fuel Cells*, K. Eguchi, S. C. Singhal, H. Yokokawa, and J. Mizusaki, Editors, PV2007-7, p. 1339, The Electrochemical Society Proceedings Series, Pennington, NJ (2007).
8. A.-L. Sauvet, J. Fouletier, F. Gaillard, and M. Primet, *J. Catal.*, **209**, 25 (2002).
9. B. D. Madsen and S. A. Barnett, *Solid State Ionics*, **176**, 2545 (2005).
10. Y. Lin and S. A. Barnett, *Electrochem. Solid-State Lett.*, **9**, A285 (2006).
11. K. Yamaji, Y. Xiong, T. Horita, N. Sakai, and H. Yokokawa, in *Seventh International Symposium on Solid Oxide Fuel Cells*, H. Yokokawa and S. C. Singhal, Editors, PV2001-16, p. 413, The Electrochemical Society Proceedings Series, Pennington, NJ (2001).
12. B. D. Madsen and S. A. Barnett, *J. Electrochem. Soc.*, **154**, B501 (2007).
13. D. L. King, J. J. Strohm, X. Wang, K. P. Recknagle, P. Singh, and Y. Wang, in *Solid State Energy Conversion Alliance (SECA) Meeting*, National Energy Technology Laboratory, U.S. Department of Energy (2006).
14. D. L. King, J. J. Strohm, X. Wang, H.-S. Roh, C. Wang, Y.-H. Chin, Y. Wang, Y. Lin, R. Rozmiarek, and P. Singh, *J. Catal.*, **258**, 356 (2008).
15. S. Linderoth, N. Bonanos, K. Jensen, and J. B. Bilde-Sorensen, *J. Am. Ceram. Soc.*, **84**, 2652 (2004).
16. J. Sfeir, P. A. Buffat, P. Mockli, N. Xanthopoulos, R. Vasquez, H. J. Mathieu, J. Vanherle, and K. R. Thampi, *J. Catal.*, **202**, 229 (2001).
17. A. L. Sauvet and J. T. S. Irvine, *Solid State Ionics*, **167**, 1 (2004).
18. K. M. Ostyn, C. B. Carter, M. Koehne, H. Falke, and H. Schmalzried, *J. Am. Ceram. Soc.*, **67**, 679 (1984).
19. D. L. Ricoult and H. Schmalzried, *J. Mater. Sci.*, **22**, 2257 (1987).
20. H. Schmalzried and M. Backhaus-Ricoult, *Prog. Solid State Chem.*, **22**, 1 (1993).
21. J. Sfeir, *J. Power Sources*, **118**, 276 (2003).
22. N. Sakai, T. Horita, K. Yamaji, Y. P. Xiong, H. Kishimoto, M. E. Brito, and H. Yokokawa, *Solid State Ionics*, **177**, 1933 (2006).
23. N. Sakai, K. Yamaji, T. Horita, M. Ishikawa, H. Yokokawa, and M. Dokiya, in *Fifth International Symposium on Solid Oxide Fuel Cells*, U. Stimming, S. C. Singhal, H. Tagawa, and W. Lehnert, Editors, PV 97-18, p. 1283, The Electrochemical Society Proceedings Series, Pennington, NJ (1997).
24. J. A. Venables, G. D. T. Spiller, and M. Hanbucken, *Rep. Prog. Phys.*, **47**, 399 (1984).
25. J. Rossmeisl and W. G. Bessler, *Solid State Ionics*, **178**, 1694 (2008).